# High-energy surface and volume plasmons in nanopatterned sub-10-nm aluminum nanostructures

*Richard G. Hobbs*[1†], *Vitor R. Manfrinato*[1†], *Yujia Yang*[1†], *Sarah A. Goodman*[1†], *Lihua Zhang*[2], *Eric A. Stach*[2], *and Karl K. Berggren*[1]

[1]Research Laboratory of Electronics, Massachusetts Institute of Technology, Cambridge, Massachusetts 02139, United States

[2]Center for Functional Nanomaterials, Brookhaven National Laboratory, Upton, New York 11973, United States

*To whom correspondence should be addressed: Tel: +1 617-258-9250; E-mail: berggren@mit.edu

**Keywords:** volume plasmon; aluminum; nanodisk; EELS; UV plasmonics; lithography.

In this work, we use electron energy-loss spectroscopy to map the complete plasmonic spectrum of aluminum nanodisks with diameters ranging from 3 nm to 120 nm fabricated by high-resolution electron-beam lithography. Our nanopatterning approach allows us to produce localized surface plasmon resonances across a wide spectral range spanning 2-8 eV. Electromagnetic simulations using the finite element method support the existence of dipolar, quadrupolar and hexapolar surface plasmon modes as well as centrosymmetric breathing modes depending on the location of the electron-beam excitation. In addition, we have developed an

approach using nanolithography that is capable of meV control over the energy and attosecond control over the lifetime of volume plasmons in these nanodisks. The precise measurement of volume plasmon lifetime may also provide an opportunity to probe and control the DC electrical conductivity of highly confined metallic nanostructures. Lastly, we show the strong influence of the nanodisk boundary in determining both the energy and lifetime of surface plasmons and volume plasmons locally across individual aluminum nanodisks, and we have compared these observations to similar effects produced by scaling the nanodisk diameter.

High-energy plasmonic nanostructures resonant in the ultraviolet (UV) to vacuum ultraviolet (VUV) region of the spectrum offer routes to channel high-energy radiation into nanoscale volumes thus supporting enhancement of high-energy photochemical reaction pathways at targeted nanoscale locations. Plasmonic nanoparticles resonant at visible and near-infrared frequencies have been used to direct electromagnetic radiation into sub-wavelength volumes known as 'hot spots', lending these nanoparticles to applications in nanoengineered devices for spectroscopy,[1–4] catalysis,[5,6] photodetectors,[7,8] sensors,[9–11] optoelectronics,[12,13] nano-optics,[14–16] photocathodes[17–19] and energy harvesting.[20,21] Consequently, high-energy plasmonic nanoparticles may provide a route to extend the spectral range of these applications into the VUV, an energy range where simple gas-phase molecules such as CO, $O_2$ and $H_2O$ have electronic absorption bands[22,23] and work functions in solids can be overcome producing reactive photoelectrons.

Plasmons in materials take one of two forms: (1) volume plasmons (VPs), which are high-energy longitudinal oscillations of conduction and valence band electrons that propagate through the bulk of a material; and (2) interface plasmons, which are collective oscillations of free electrons at an interface. When an interface plasmon occurs at the surface of a material it is referred to as a surface plasmon (SP). SPs can adopt multiple forms, those being surface plasmon polaritons (SPPs), which are propagating SPs that exist at the interface between a metal and a dielectric, and localized surface plasmon resonances (LSPRs) that exist on sub-wavelength metallic nanoparticles.

Controlled engineering of LSPRs and VPs with energies greater than 5 eV has been limited to date,[24–34] partly due to the fact that conventional plasmonic metals such as Au and Ag operate in the visible to near-infrared region of the spectrum, but also due to the requirement for fabrication and spectroscopic methods capable of sub-10-nm spatial resolution to control and characterize these higher energy plasmons. Consequently, the development of plasmonic systems and devices operating in the deep or vacuum UV has been inhibited. Plasmonic systems operating in the UV region of the spectrum would support advances in UV nano-optics for lithography,[35] photochemistry in the UV,[36] and plasmon-enhanced sensing and spectroscopy in the UV.[37,38]

The VP energy ($\hbar\omega_\mathrm{p}$) of Al is 15 eV and consequently it can theoretically support SPs with energies as high as 10.5 eV $\left(\frac{\hbar\omega_p}{\sqrt{2}}\right)$ at a planar boundary or 8.6 eV $\left(\frac{\hbar\omega_p}{\sqrt{3}}\right)$ on a spherical particle.[39] Moreover, Al is cheap and abundant in the earth's crust, making it a suitable candidate for low-cost plasmonic devices when integrated with a cost-effective patterning process. As a result, Al has been the subject of a number of investigations recently with the goal of developing plasmonic materials that are capable of enhancing light-matter interactions at UV to VUV wavelengths.[28,29,31,40–43] The production of Al nanostructures exhibiting high-energy SP modes to channel UV light into sub-wavelength regions requires flexible nanofabrication methods capable of producing sub-20-nm structures. High-resolution electron-beam lithography fulfills such criteria and enables the fabrication of sub-20-nm nanostructures on a variety of substrates for device integration.[44–48]

Our recent ability to nanofabricate structures at the sub-10-nm length scale[44,45,47,49–51] suddenly presents the prospect of lithographically engineering structures for the modification of VP resonances, while simultaneously enabling the development of high-energy SPs. VPs constitute one of the major energy-loss avenues for charged-particle beams in matter. Moreover, the VP peak in Al has recently been exploited to measure temperature in an active microelectronic device on the nanometer length scale[48] emphasizing the importance of a full understanding of VP behavior in nanostructures. In our previous work, we outlined a detailed analysis of the VP-mediated transfer of energy from an energetic electron beam to chemical transformations in thin films of an electron-beam-sensitive material.[49] We observed that VPs decay over distances of 1-10 nm, thus highlighting the importance of nanofabrication capabilities on the single-nanometer length scale.

Here we demonstrate control of both VP and LSPR energy and lifetime in Al nanodisks – as measured using scanning transmission electron microscopy (STEM) and electron energy-loss spectroscopy (EELS) – by tuning the dimensions of nanodisks from the 100-nm-length scale to below 10 nm using electron-beam lithography. STEM systems equipped with EELS modules provide a route to study VPs and LSPRs with the requisite spatial (~ 1 nm) and energy resolution (~ 100 meV) needed to probe their behavior near interfaces and within sub-10-nm particles.[52–57] Our approach combining high-resolution electron-beam lithography, STEM and EELS (see supporting information for details of fabrication, microscopy and spectroscopy) allowed us to control the VP relaxation time in the range of 500-750 as (attoseconds) and observe that the relaxation time increased with increasing nanodisk diameter. We have also observed an increase in the energy of the Al VP resonance with decreasing nanodisk diameter as well as a blue shift in the VP peak as the excitation probe (a sub-nanometer-diameter electron beam) is brought to within 10 nm of the nanodisk perimeter. Models based on a non-local dielectric response, which were reported previously can describe both of these observations.[58,59] Moreover, we also controlled the energy of SP excitations in the 2-8 eV range and have correlated the observed peaks in the SP spectra to specific plasmon modes by numerical modeling using the finite element method. The spatial distributions of all plasmon modes on Al nanodisks were measured with nanometer resolution using STEM-EELS, including determination of changes in plasmon energy, intensity and lifetime. The results outlined in this work may offer a route to extend the reach of plasmonic devices to the ~10 eV scale.

Figure 1 outlines our experimental approach to investigate SPs and VPs in Al nanostructures. We fabricated Al nanodisks with metallic core-diameters ranging from 3 nm to greater than 100 nm on ultrathin 5 to 10-nm-thick $SiN_x$ membranes by electron-beam lithography. Details of the fabrication process are available in section 1 of the supporting information. Figure 1a shows an example bright-field transmission electron micrograph of 6-nm-diameter (including native surface oxide) Al nanodisks fabricated by this method. The Al nanodisks fabricated in this work are typically polycrystalline in nature. Figure S11 in the supporting information shows an image of nanodisks having diameter > 100 nm, which clearly shows the polycrystallinity of the nanodisks with crystal grains typically measuring ~ 10 nm. We mapped plasmon excitations across these nanodisks with nanometer-resolution using STEM and EELS as shown schematically in figure 1b. Further details related to EELS acquisition are included in section 2 of the supporting information. Figure 1c shows an example high-angle annular dark-field (HAADF) STEM image of a 17-nm-diameter Al nanodisk. An electron energy-loss (EEL) spectrum was acquired at each 1-nm$^2$ pixel in parallel to image acquisition to produce a 3-d spectrum image. Figure 1d shows an example of an EEL spectrum acquired from a pixel near the center of an Al nanodisk. The spectrum clearly shows peaks that can be assigned to SP and VP excitations, as well as the elastic or zero-loss peak (ZLP) at 0 eV. The ZLP can be subtracted from all spectra acquired, leaving spectra that contain the relative intensity of inelastic loss pathways in the sample. This technique allows us to choose a specific inelastic loss pathway by selecting an energy band in each spectrum and subsequently plotting the intensity of that loss pathway as a function of position on the sample. Consequently, we produced maps of SPs and VPs in the 0-50 eV energy-loss range with nanometer resolution. Details of methods used to subtract the ZLP and extract the intensities, energies and spectral linewidths of each loss pathway are included in section 3 of the supporting information. Results produced using this mapping technique are described in the subsequent sections of this manuscript.

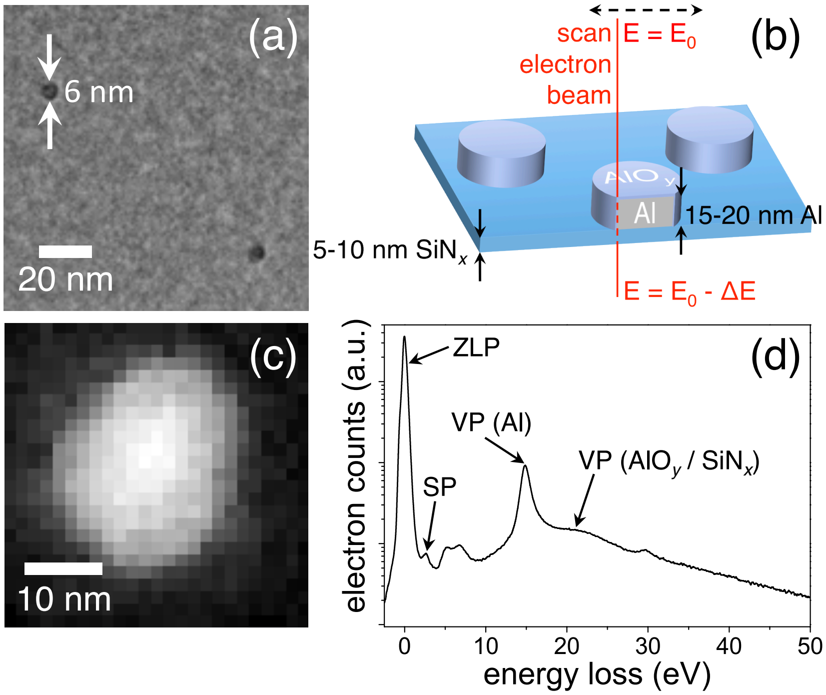

**Figure 1.** Experimental approach. (a) Bright-field TEM micrograph of 15-20-nm-thick Al nanodisks fabricated on 5-nm-thick SiN$_x$ membranes by electron-beam lithography. (b)

Schematic representation of the spectral imaging EELS approach used to map plasmonic modes in Al nanostructures. The incoming electron has energy $E_0$ = 200 keV and the transmitted electron loses energy $\Delta E$. Spectrum images are generated by plotting energy-loss against intensity at each pixel on a 2-d square array forming a 3-d data set ($x$ position, $y$ position, energy-loss). (c) HAADF-STEM image of an Al nanodisk acquired in parallel to the spectral image. A step size of approximately 1 nm was typically employed during acquisition of spectrum images. (d) An example of a raw EEL spectrum acquired from the center of an Al nanodisk in this work. The intensity (plotted on a log scale) of the ZLP (zero-loss peak), SP peak of Al, VP peaks of Al, $SiN_x$ and $AlO_y$ are visible here.

Figure 2 shows the results of our detailed analyses of SP excitations in Al nanodisks. In order to push SP modes to the highest energies and achieve wider SP spectral control, we fabricated Al nanodisks with varying diameters and mapped SP excitations using the spectrum imaging technique described in figure 1. Figure 2a shows an example SP EEL spectrum acquired from a 110-nm-diameter Al nanodisk when the electron beam was placed at the nanodisk boundary. The boundary is defined as the position where the intensity of the Al VP peak drops below the noise floor as the electron beam is scanned outward from the center of the nanodisk. This position represents the edge of the metallic Al, which is responsible for the plasmonic properties of these nanodisks. The spectrum shown in figure 2a was processed to subtract the background due to the ZLP and VP peaks. We compared the experimental results to the results of numerical simulations shown in figure 2b. Details of the method used to simulate the EELS spectra are included in section 4 of the supporting information. Several SP peaks are present, which we have labeled in order of increasing energy (SP1, SP2, SP3 etc.). Three Gaussian peaks representing SP1-3 were fit to the experimental spectrum in the 1.5-6.0 eV range as shown in figure 2a. The relative positions of the fitted peaks compare well with the simulated spectrum, although all fitted peaks were blue-shifted with respect to the simulated peaks by approximately 0.3-0.4 eV. This shift could be related to a difference between the oxide thickness used in simulations (2.6 nm) and that produced experimentally, or due to a difference between the simulated and experimental geometries of the nanodisk. A blue-shift in the experimental spectrum with respect to the simulated spectrum would be expected if the native oxide layer is thinner than that simulated, if the oxide layer or substrate has a lower than expected refractive index, if the fabricated disk is marginally smaller than that simulated or if the nanodisk accumulated charge from the electron beam during acquisition of the spectrum. The peaks in the simulated spectra are also narrower than those observed experimentally. Convolution of the simulated spectrum in figure 2b with a Gaussian peak (350 meV FWHM) representing the ZLP results in a simulated spectrum that more closely resembles that measured experimentally, as shown in figure S9. Figures 2c and 2d show experimentally measured and simulated EEL spectra respectively for the case where the electron beam is placed at the center of the 110-nm-diameter nanodisk. The measured spectrum in figure 2c clearly shows energy loss at higher energies than observed when the beam was placed at the boundary (figure 2a). The simulated spectrum in figure 2d supports the presence of plasmon modes at higher energies than for the boundary excitation. The simulated spectrum predicts LSPR modes at the center of the nanodisk in the 4-8 eV range, which we have labeled CP1, CP2 and CP3. Four Gaussian peaks were fit to the experimental spectrum in figure 2c, and the relative positions of these four peaks were found to compare well with the simulated spectrum; however, just as was observed for figure 2a both CP1 and CP2 peaks were blue-shifted by 0.3-0.4 eV. The fitted peak representing CP3 was observed at the same energy to that simulated (7.2 eV). Figure 2e shows maps of the simulated surface fields on a 120-nm-diameter

Al nanodisk associated with SP1-3 and CP1-3, and the surface fields on a 20-nm-diameter nanodisk associated with SP1 and SP2. The simulated SP1 modes show a clear dipolar character for all nanodisk dimensions simulated. The SP2 and SP3 modes display quadrupolar and hexapolar character respectively in 120-nm-diameter nanodisks; however, these modes are complicated by out-of-plane polarities for smaller diameter nanodisks as can be seen for the case of the SP2 mode on the 20-nm-diameter nanodisk in figure 2e. Surface plasmon modes CP1, CP2, and CP3 show surface field distributions characteristic of breathing plasmon modes.[60] Similar breathing mode LSPRs have been observed in silver nanodisks and they have been excited optically.[61] As such, the breathing mode plasmons observed here may offer a route to plasmon-enhanced processes in the 5-10 eV energy range. Figure 2f shows a plot of SP energy versus nanodisk diameter for various LSPR modes when the electron beam is placed at the perimeter of the nanodisk. Experimentally measured LSPR energies and simulated values compare well for the larger diameter nanodisks studied. However, mixing of plasmon modes in nanodisks with smaller diameters prevents individual modes from being clearly resolved. We have observed that lower order plasmon modes SP1-SP3 increase in energy with decreasing nanodisk diameter as predicted by electromagnetic simulations. Moreover, the distribution of measured SP energies shown in the plot in figure 2f is in agreement with the predicted distributions from simulations for nanodisks having diameters greater than 40 nm. Figure 2g shows experimentally measured and simulated values of SP energies when the electron beam was placed at the center of each nanodisk. Interestingly, as well as CP modes a peak characteristic of the dipolar SP1 mode was observed on many nanodisks when the electron beam was placed at the center of the nanodisk. The positions of the measured and simulated peaks compare well for larger nanodisks. However, for smaller nanodisk diameters, the peaks began to overlap, which makes assignment of specific plasmon modes to the experimentally measured peaks unreliable. Nevertheless, the energy distributions of the measured peaks compare well with the spectral regions where CP modes are expected.

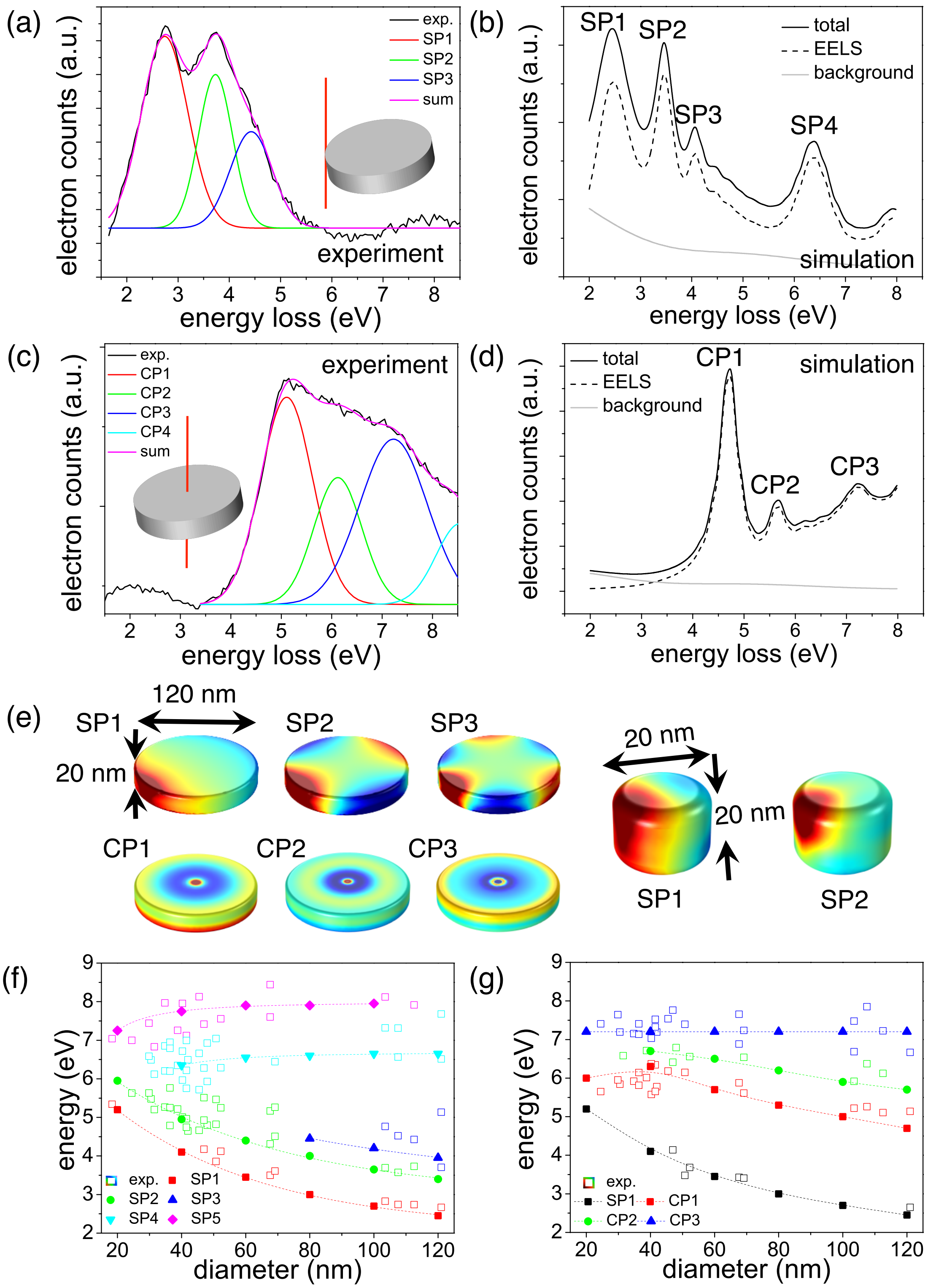

**Figure 2.** Surface plasmons (SPs) in Al nanodisks. **(a)** Experimentally measured EEL spectrum for a 110-nm-diameter Al nanodisk. The EEL spectrum was acquired when the electron beam

was at the perimeter of the nanodisk near the Al/AlO$_y$ interface as shown schematically by the red line passing by the disk in the figure. **(b)** Simulated EEL spectra obtained using the finite element method for an electron-beam excitation at the perimeter of such a nanodisk showing SP excitations in the 2-5 eV energy range, as well as a peak above 6 eV. Peaks representing SP1-3 modes were fit to the experimental data in (a) as shown by the red, green, and blue traces respectively. **(c)** Experimental EEL spectrum acquired at the center of the same nanodisk studied in (a). **(d)** Simulated spectra show that higher energy plasmons are excited at the center of the nanodisk than at the disk perimeter. These modes are labeled as center plasmon modes (CP) indicating that these surface plasmons are excited more strongly when the beam is placed at the center of the nanodisk. Peaks representing CP modes are fit to the experimental data (c). **(e)** Surface normal electric field maps for the relevant SP and CP modes in nanodisks with two different diameters. These maps are indicative of the charge-density profiles expected for each of the SP modes. SP1, SP2, and SP3 are dipolar, quadrupolar and hexapolar modes respectively, while CP1-3 are breathing modes. **(f,g)** Plots of simulated (filled data points) and experimental (open data points) energies of SP and CP peaks versus nanodisk diameter. The experimental data points have been colored to match the nearest simulated data curve allowing correlations to be drawn between experimental and simulated data. SP spectra were measured at the perimeter of nanodisks where the perimeter is defined as the point at which the intensity of the VP peak drops to zero. The error in diameter is ± 0.5 nm, and the error in energy is no more than ± 0.6 eV for all data points. The dashed lines are included as guides to the eye for the simulation results.

The results presented in figure 3 show the successful use of nanopatterning to control the energy, intensity, and lifetime of VPs in aluminum. The results suggest that nanopatterning will allow control of the VP energy with meV precision and attosecond control of the VP lifetime. Figure

3a shows a small increase of ~ 100 meV in VP energy when decreasing the nanodisk diameter. Figure 3a also shows analytical calculations of multiple VP modes (see supporting information section 5 for details), which compare well with experimental data. The agreement between the data and low-order VP modes suggests that only low-order VP modes are excited inside the Al nanodisks. Figure 3b shows a significant decrease in VP intensity with decreasing nanodisk diameter. The VP intensity was observed to scale linearly with decreasing nanodisk diameter as shown by the linear fit applied to the data in figure 3b. Extrapolation of this linear function to smaller diameters suggests that the VP intensity should drop to zero for a nanodisk with a diameter of 1.6 nm ± 0.6 nm. Figure 3c shows that there is a significant increase in the FWHM of the VP peak with decreasing nanodisk diameter. We modeled the relationship between the FWHM of the VP peak and the nanodisk diameter using the formula given in equation 1, which is based on an effective mean free path ($L_{\mathrm{eff}}$) for the VP.[62]

$$FWHM_{(\mathrm{R})} = FWHM_{(\infty)} + \hbar\nu_F / L_{\mathrm{eff(R)}} \qquad (1)$$

Here, $L_{\mathrm{eff}}$ is related to the nanodisk dimension by the expression $L_{\mathrm{eff}} = 4(\mathit{Volume})/(\mathit{Surface\ Area})$, $\mathrm{FWHM}_{(\mathrm{R})}$ is the width of the VP peak for a nanodisk and $\mathrm{FWHM}_{(\infty)}$ is the width of the VP peak for a bulk sample.[62] We obtained effective mean free paths from 1.8 nm to 9.2 nm for nanodisks with diameters from 2 nm to 14 nm and heights of 12 nm. This formula originated from a proposed dielectric constant for sub-10-nm structures, which has been verified for plasmonic metallic clusters.[62,63,33] The model is in good agreement with the data. Finally, Figure 3d shows a plot of the calculated VP relaxation time as a function of the diameter of the metallic Al core of the nanodisks. The relaxation time ($\tau$) was calculated using the expression $\tau = \hbar / FWHM_{(R)}$.[64] We note that the slope of a linear fit to the data was measured to be 18 as/nm. Assuming that the calculated relaxation time is valid and considering the 2 nm feature-size control achieved in this study (standard deviation of nanodisk diameter for a given dose is 2 nm), we are able to tune the VP relaxation time with an accuracy of 36 as. These results suggest that attosecond pulses of radiation will be required to probe collective electron excitations represented by volume plasmons. Moreover, as Batson showed previously[33] the DC conductivity can be estimated from measurement of the VP relaxation. Consequently, precise control of the VP lifetime may allow precise control of the DC conductivity locally on the nanoscale, which will have applications in areas such as metallic-interconnects design at sub-10-nm dimensions.

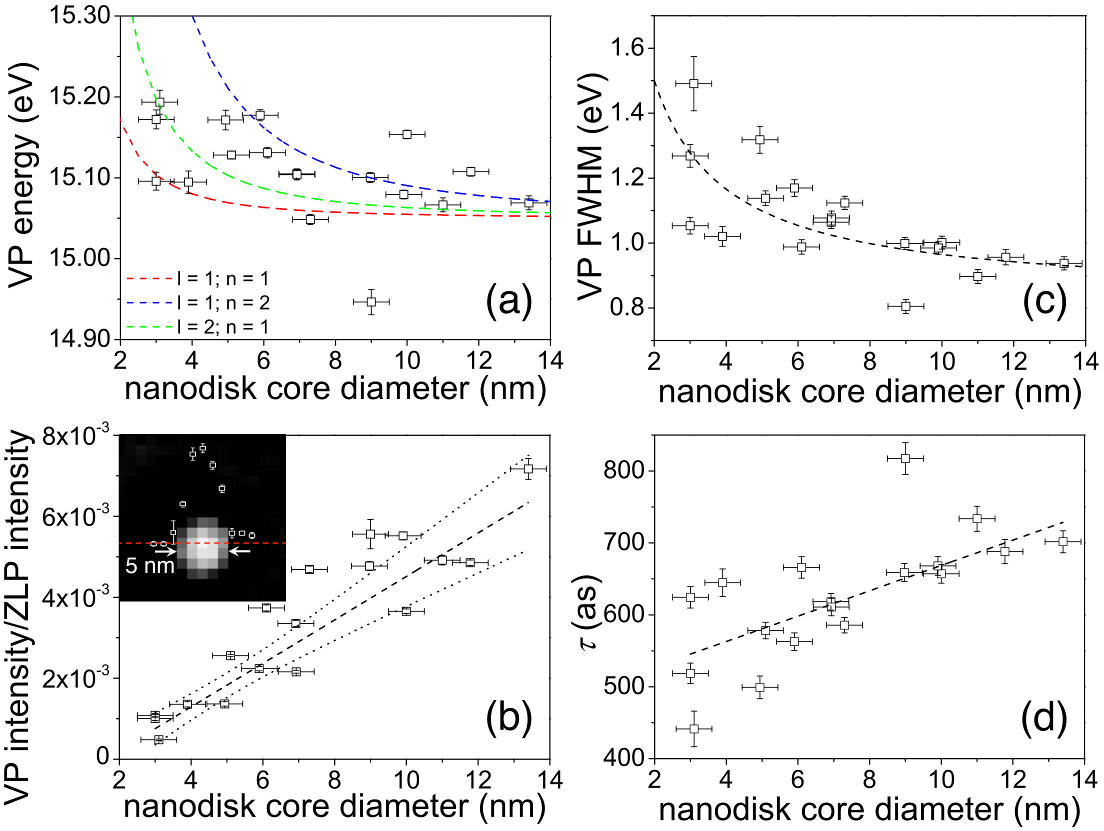

**Figure 3.** Volume plasmons. The figure shows the dependence of VP peak energy, intensity, FWHM, and relaxation time on nanodisk diameter. All measurements were collected at the central region of nanodisks where VP intensity is strongest. **(a)** VP peak energy at the center of nanodisks as a function of nanodisk core diameter. Dashed lines represent results of an analytical

model for VP standing waves confined in nanodisks (all with quantum number $m = 0$; see supporting information).[59] The dashed red line represents the $l = 1$ mode with lowest wavevector ($n = 1$); the blue dashed line is the $l = 1$ mode with second lowest wavevector ($n = 2$), and the green dashed line is the $l = 2$ mode with lowest wavevector ($n = 1$). The model suggests excitation of low-order standing wave VPs. **(b)** Ratio of the VP intensity (peak intensity with background subtracted) and the ZLP intensity at the center of nanodisks as a function of core diameter. A linear fit to the experimental data ($R^2 = 0.82$) suggests that VP intensity goes to zero for nanodisks with diameters of 1.6 ± 0.6 nm. The thick dashed line represents a linear fit to the measured data, while the thin dashed lines represent bounds of 95% confidence. Inset, VP intensity as a function of electron-beam position on a 5-nm-diameter nanodisk. White squares represent the intensity recorded at pixels along the red dashed line. **(c)** VP full width at half maximum (FWHM) as a function of the core diameter of the nanodisks. The dashed line represents a model of VP FWHM as a function of diameter considering the effective mean free path ($L_{\mathrm{eff}}$) of electrons in a nanodisk as described in the text. The model fits the data with a value of $R^2 = 0.37$. **(d)** Calculated VP relaxation time ($\tau$) as a function of nanodisk core diameter. Dashed line represents a linear fit to the data shown as a guide to the eye ($R^2 = 0.52$). The slope of the linear fit was 18 ± 4 as/nm.

The results shown in figure 4 demonstrate the significant role played by the nanodisk perimeter in determining the local energy, intensity and lifetime of both SP and VP excitations, on the single-nanometer level across an Al nanodisk with a 12-nm-diameter metallic core. Figures 4a-d show a high-angle annular dark-field (HAADF) image of the nanodisk, a map of the Al VP intensity, a map of the Al SP intensity and a color map of the Al VP, Al SP and $AlO_y$ VP, respectively. All maps were prepared with 1 nm pixels. Figures 4e-h show plots of the Al SP and

VP intensity, Al SP and VP energy, Al VP FWHM and energy, and the Al VP and SP together with the $AlO_y$ VP, respectively, as a function of position on a line-scan through the center of the nanodisk. These plots can be used to study the behavior of the VP and SP at the Al-$AlO_y$ interface. The boundary effect at this interface consists of a modification of the VP resonance due to interaction with SPs. In this work, we have observed that the VP intensity is nominally constant at the center of nanodisks greater than 20 nm in diameter. However, the VP intensity begins to decay exponentially at a threshold distance inside the boundary. This threshold distance can be described classically in terms of Bohr's delocalization distance $b_{\max} = v/\omega_p$, where ν is the velocity of the incident electron and $\omega_p$ is the angular frequency of the volume plasmon.[64] Bohr's delocalization distance represents the maximum distance at which inelastic scattering can occur from an electrostatic scattering source, e.g. an atomic nucleus or a free-electron, measured in terms of the impact parameter $b$. Hence, $b_{\max}$ is the threshold impact parameter below which the SP will rise in intensity at the expense of the VP intensity. A 200 keV electron has a velocity of $2.086 \times 10^8$ $ms^{-1}$, and the energy of the VP in Al is ≈ 15 eV, resulting in $b_{\max} = 9.2$ nm. Consequently, the VP intensity is expected to reach a maximum at an impact parameter of $b_{\max}$ from the boundary toward the nanodisk center. Figure 4e shows that the VP intensity increases with distance from the boundary, but in this case does not saturate, as the nanodisk radius is less than $b_{\max}$. Figure 4e also shows that there is a commensurate increase in SP intensity and decrease in VP intensity as the beam approaches the boundary. This relationship between SP and VP intensities near the boundary is due to a conservation of oscillator degrees of freedom at the boundary, which dictates that the sum of oscillator strengths for all plasmons (SP and VP) is constant.[65] Figure 4f shows that the peak energies of both the SP and VP peaks blue shift approaching the boundary. The nonlocal hydrodynamic model used to explain the increase in VP energy with decreasing nanodisk diameter, as shown in figure 3a, may also be used to predict an increase in VP and SP energy near the boundary.[58] Figure 4g shows that the VP energy and lifetime (~ 1/FWHM) are altered near the boundary of the nanodisks. The change in VP energy and lifetime at the boundary matches qualitatively with the diameter-dependence observed in figure 3. The VP energy and FWHM increase with decreasing nanodisk diameter, and likewise the VP energy and FWHM increase at the boundary. The boundary effect dominates at reduced nanodisk diameters where the boundary regions make up a larger fraction of the nanodisk and as such it is likely to contribute to the observed diameter dependence in the VP energy and FWHM. Figure 4h shows that the Al SP intensity peaks at the Al-AlO$_y$ interface as might be expected. The figure also shows that the AlO$_y$ layer on the sidewall of the nanodisk is slightly thicker on the right hand side of the nanodisk. The slight increase in oxide thickness manifests itself as a slight increase in surface plasmon damping, resulting in a reduced SP intensity on the right hand side of the nanodisk.[28] The correlation between reduced oxide thickness and increased local SP intensity has been observed on several nanodisks (see figure S7) and suggests that variation in oxide thickness across individual nanostructures will significantly affect the intensity of the LSPR. There also appears to be a slight increase in the Al VP intensity across the core of the nanodisk, which suggests that the Al disk may not be uniformly thick across its width and might explain the asymmetric Al VP intensity across the core of the nanodisk. Recent works have begun to investigate the spatial distribution of plasmonic excitations in three dimensions using tomographic methods and these works represent an important step toward a complete understanding of plasmonic systems at close to the atomic scale.[57,66] Further discussion of the role of thickness variation and surface roughness on VP intensity in our work, including analysis of HAADF-STEM images is included in section 6 of the supporting information (see figures S10, S16 and S17).

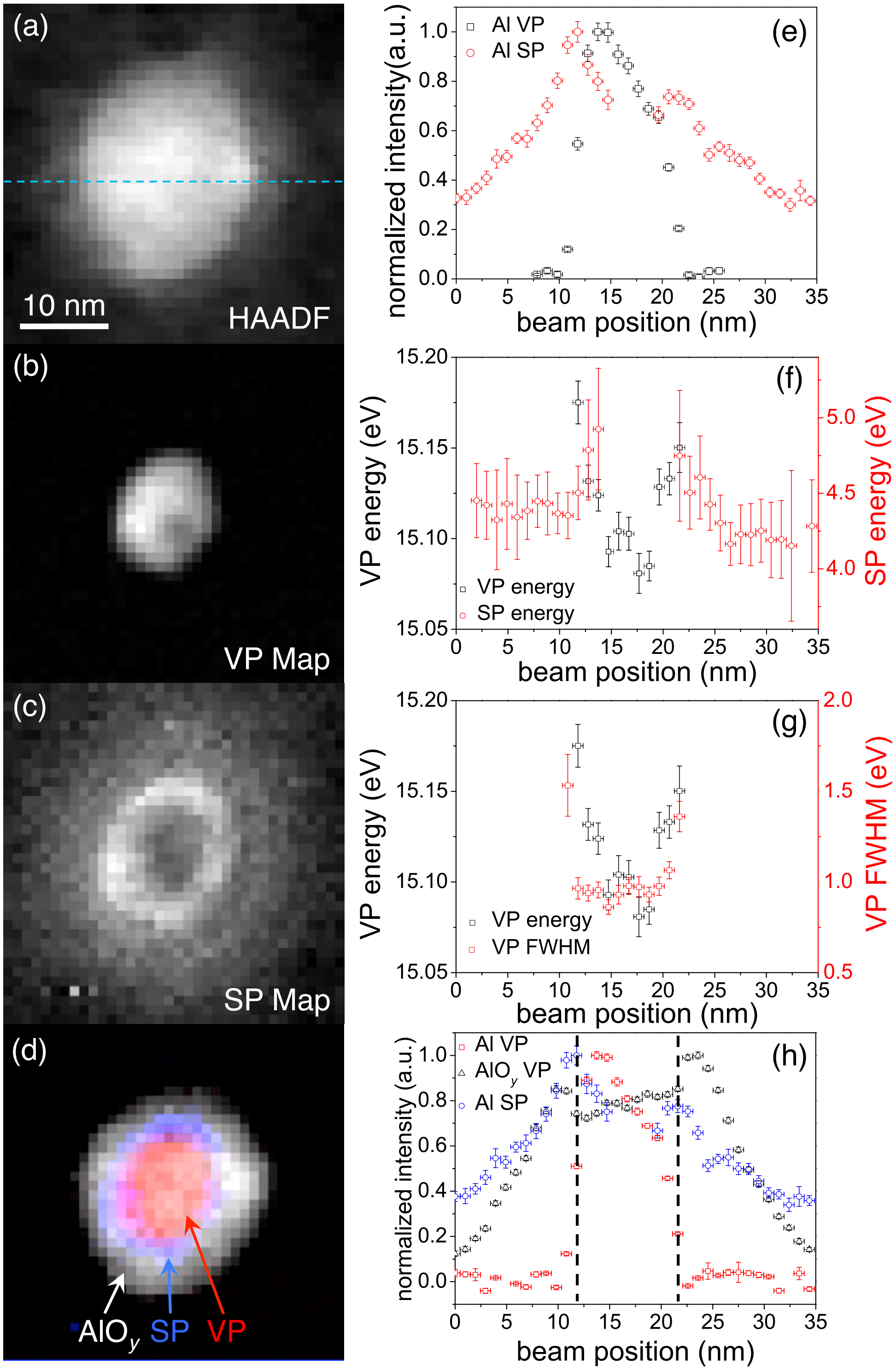

**Figure 4.** The boundary-effect. **(a)** High-angle annular dark-field (HAADF) scanning transmission electron micrograph of a 12-nm-diameter Al nanodisk. The blue dashed line

represents the electron beam path in (e-h). The scale bar applies to all of the images (a-d). **(b)** EEL map acquired at the VP energy (13-17 eV) after background subtraction. **(c)** EEL map acquired at the SP1 energy (2.85-5.3 eV) for the same nanodisk. The gray-scale level in (b) and (c) is proportional to the integral of the area under the VP peak and SP peak of Al respectively. (d) Color map displaying the distribution of electron energy-loss characteristic of interaction with VP, SP1, and $AlO_y$ regions. (e) Normalized SP1 and VP intensities plotted as a function of the position of the electron-beam on a 12-nm-diameter nanodisk. The VP intensity decays exponentially near the Al-$AlO_y$ boundary. (f) VP and SP1 energy as a function of electron-beam position on the same nanodisk analyzed in (e). The VP energy was observed to increase as the beam approached the edge of the nanodisk from the center of the nanodisk. (g) VP energy and FWHM as a function of beam position. Both VP energy and FWHM increase as the beam approaches the edge of the particle. While a decrease in thickness at the edge of the particle may partially contribute to a decrease in VP intensity, the increase in VP energy and FWHM is a result of the boundary effect. (h) Plot of normalized intensity of electron energy-loss peaks for the Al VP, Al SP1, and $AlO_y$ VP excitations versus the position of the electron beam along the diameter of the nanodisk in (a). The dashed black line represents the position of the Al-$AlO_y$ interface.

In this work, we have accurately measured and modeled the behavior of LSPRs and VPs in Al nanodisks ranging from 3-120 nm in diameter. Our study has shown that the VP energy and FWHM increase both at the boundary of Al nanodisks and with decreasing nanodisk diameter. We have explained this behavior of VP energy and FWHM with models based on low-order VP standing waves and dimensional scaling of the VP mean free path respectively, and we have provided a qualitative explanation based on the boundary effect. However, a universal model that fully explains our system is still lacking. We have observed that the behavior of VPs at the sub-10 nm scale can be explained by the increased contribution of the boundary at these length scales and that a model based on the nonlocal material response and the formation of low-order VP standing waves is in agreement with our measurements. The evidence provided here will help to direct future studies of electron interactions with matter on the nanoscale. For example, given the role of VPs in determining the resolution of electron-beam lithography (EBL),[49] one potential application of this work would be in the synthesis of nanostructured EBL resists that achieve higher resolution by suppressing VP excitation.[67,68] Moreover, the correlation between the VP relaxation time and the DC conductivity suggests that the methods used to measure and control the VP relaxation time here, may also be used to probe and control the DC conductivity on the nanometer level. Additionally, as the plasmon excitations studied and controlled here ranged from 2-15 eV in energy, these results will support the development of plasmon-enhanced processes, metamaterials and metasurfaces operational from the UV to the VUV. We observed LSPRs ranging in energy from 2-10 eV, and we have assigned those LSPRs to a variety of multipolar and breathing modes. These LSPRs may be used to channel light into nanoscale volumes and enhance photochemical processes across this energy range. Optical excitation of VPs under certain confined dimensions has also been demonstrated previously.[69] Therefore, engineering VPs may extend the tailoring of light-matter interactions to even higher energies.

## Author Contributions

[†] These authors contributed equally to this work.

## Acknowledgements

This research used the Hitachi HD2700C STEM at the Center for Functional Nanomaterials, which is a U.S. DOE Office of Science Facility, at Brookhaven National Laboratory under Contract No. DE-SC0012704. RGH, VRM, YY, and KKB would like to also acknowledge support from the Gordon and Betty Moore Foundation. SAG was supported by the Department of Defense (DoD) through the National Defense Science & Engineering Graduate Fellowship (NDSEG) Program. We thank James Daley and Mark Mondol for assistance and advice related to nanodisk fabrication. We also would like to thank Prof. Philip Batson for helpful discussions and assistance with measurements at Rutgers University.

## Notes

The authors declare no competing financial interests.

## Supporting Information

Further details related to fabrication of nanodisks, EELS acquisition, processing of EELS spectra, simulation of surface plasmon excitations, and the analytical model used to describe volume plasmons are included in the supporting information. The supporting information also includes HAADF STEM micrographs of all nanodisks studied in this work as well as results of AFM analysis of surface roughness and analysis of (S)TEM micrographs for selected nanodisks. This information is available free of charge via the Internet at http://pubs.acs.org.

## References

(1) Willets, K. A.; Van Duyne, R. P. *Annu. Rev. Phys. Chem.* **2007**, *58*, 267–297.

(2) Duan, H.; Hu, H.; Kumar, K.; Shen, Z.; Yang, J. K. W. *ACS Nano* **2011**, *5*, 7593–7600.

(3) Ye, J.; Wen, F.; Sobhani, H.; Lassiter, J. B.; Dorpe, P. Van; Nordlander, P.; Halas, N. J.

*Nano Lett.* **2012**, *12*, 1660–1667.

(4) Zijlstra, P.; Paulo, P. M. R.; Orrit, M. *Nat. Nanotechnol.* **2012**, *7*, 379–382.

(5) Linic, S.; Aslam, U.; Boerigter, C.; Morabito, M. *Nat. Mater.* **2015**, *14*, 567–576.

(6) Brongersma, M. L.; Halas, N. J.; Nordlander, P. *Nat. Nanotechnol.* **2015**, *10*, 25–34.

(7) Hu, X.; Dauler, E. A.; Molnar, R. J.; Berggren, K. K. *Opt. Express* **2011**, *19*, 17–31.

(8) Knight, M. W.; Sobhani, H.; Nordlander, P.; Halas, N. J. *Science* **2011**, *332*, 702–704.

(9) Ostovar, S.; Rocks, L.; Faulds, K.; Graham, D.; Parcha, V.; Bou, P.; Blanch, E. W. *Nat. Chem.* **2015**, *7*, 591–596.

(10) Anker, J. N.; Hall, W. P.; Lyandres, O.; Shah, N. C.; Zhao, J.; Van Duyne, R. P. *Nat. Mater.* **2008**, *7*, 442–453.

(11) Nicoli, F.; Verschueren, D.; Klein, M.; Dekker, C.; Jonsson, M. P. *Nano Lett.* **2014**, *14*, 6917–6925.

(12) Bergman, D. J.; Stockman, M. I. *Phys. Rev. Lett.* **2003**, *90*, 027402.

(13) Cai, W.; Vasudev, A. P.; Brongersma, M. L. *Science* **2011**, *333*, 1720–1723.

(14) Barnes, W. L.; Dereux, A.; Ebbesen, T. W. *Nature* **2003**, *424*, 824–830.

(15) Maier, S. A.; Kik, P. G.; Atwater, H. A.; Meltzer, S.; Harel, E.; Koel, B. E.; Requicha, A. A. G. *Nat. Mater.* **2003**, *2*, 229–232.

(16) Schuller, J. A.; Barnard, E. S.; Cai, W.; Jun, Y. C.; White, J. S.; Brongersma, M. L. *Nat. Mater.* **2010**, *9*, 193–204.

(17) Hobbs, R. G.; Yang, Y.; Fallahi, A.; Keathley, P. D.; De Leo, E.; Kaertner, F. X.; Graves, W. S.; Berggren, K. K. *ACS Nano* **2014**, *8*, 11474–11482.

(18) Dombi, P.; Horl, A.; Racz, P.; Marton, I.; Trugler, A.; Krenn, J. R.; Hohenester, U. *Nano Lett.* **2013**, *13*, 674–678.

(19) Polyakov, A.; Senft, C.; Thompson, K. F.; Feng, J.; Cabrini, S.; Schuck, P. J.; Padmore, H. A.; Peppernick, S. J.; Hess, W. P. *Phys. Rev. Lett.* **2013**, *110*, 076802.

(20) Sheldon, M. T.; van de Groep, J.; Brown, A. M.; Polman, A.; Atwater, H. A. *Science* **2014**, *346*, 828–831.

(21) Linic, S.; Christopher, P.; Ingram, D. B. *Nat. Mater.* **2011**, *10*, 911–921.

(22) Wolf, M.; Nettesheim, S.; White, J. M.; Hasselbrink, E.; Ertl, G. *J. Chem. Phys.* **1991**, *94*, 4609–4619.

(23) McNesby, J. R.; Okabe, H. *Adv. Photochem.* **1964**, *3*, 157–240.

(24) Kociak, M.; Mahfoud, Z.; Proust, J. *Nano Lett.* **2014**, *14*, 5517–5523.

(25) King, N. S.; Liu, L.; Yang, X.; Cerjan, B.; Everitt, H. O.; Nordlander, P.; Halas, N. J. *ACS Nano* **2015**, *9*, 10628–10636.

(26) McClain, M. J.; Schlather, A. E.; Ringe, E.; King, N. S.; Liu, L.; Manjavacas, A.; Knight, M. W.; Kumar, I.; Whitmire, K. H.; Everitt, H. O.; Nordlander, P.; Halas, N. J. *Nano Lett.* **2015**, *15*, 2751–2755.

(27) Martin, J.; Kociak, M.; Mahfoud, Z.; Proust, J.; Gérard, D.; Plain, J. *Nano Lett.* **2014**, *14*, 5517–5523.

(28) Knight, M. W.; King, N. S.; Liu, L.; Everitt, H. O.; Nordlander, P.; Halas, N. J. *ACS Nano* **2014**, *8*, 834–840.

(29) Bisio, F.; Zaccaria, R. P.; Moroni, R.; Maidecchi, G.; Alabastri, A.; Gonella, G.; Giglia,

A.; Andolfi, L.; Nannarone, S.; Mattera, L.; Canepa, M. *ACS Nano* **2014**, *8*, 9239–9247.

(30) Zoric, I.; Zach, M.; Kasemo, B.; Langhammer, C. *ACS Nano* **2011**, *5*, 2535–2546.

(31) Knight, M. W.; Liu, L.; Wang, Y.; Brown, L.; Mukherjee, S.; King, N. S.; Everitt, H. O.; Nordlander, P.; Halas, N. J. *Nano Lett.* **2012**, *12*, 6000–6004.

(32) Wang, Y. W.; Kim, J. S.; Kim, G. H.; Kim, K. S. *Appl. Phys. Lett.* **2006**, *88*, 143106.

(33) Batson, P. E. *Solid State Commun.* **1980**, *34*, 477.

(34) Nienhaus, H.; Kravets, V.; Koutouzov, S.; Meier, C.; Lorke, A.; Wiggers, H.; Kennedy, M. K.; Kruis, F. E. *J. Vac. Sci. Technol. B* **2006**, *24*, 1156–1161.

(35) Smith, B. W. *Proc. SPIE* **2009**, *7274*, 1–10.

(36) Zhou, L.; Zhang, C.; McClain, M.; Manjavacas, A.; Krauter, C. M.; Tian, S.; Berg, F.; Everitt, H. O.; Carter, E. A.; Nordlander, P.; Halas, N. J. *Nano Lett.* **2016**, *16*, 1478–1484.

(37) Asher, S. A. *Annu. Rev. Phys. Chem.* **1988**, *39*, 537–588.

(38) Jha, S. K.; Ahmed, Z.; Agio, M.; Ekinci, Y.; Loffler, J. F. *J. Am. Chem. Soc.* **2012**, *134*, 1966–1969.

(39) Ritchie, R. H. *Phys. Rev.* **1957**, *106*, 874–881.

(40) Langhammer, C.; Schwind, M.; Kasemo, B.; Zoric, I. *Nano Lett.* **2008**, *8*, 1461–1471.

(41) Peng, S.; Liu, W.-G.; Jaramillo-Botero, A.; Goddard, W. A.; Atwater, H. A. *Appl. Phys. Lett.* **2015**, *106*, 023102.

(42) Martin, J.; Plain, J. *J. Phys. D. Appl. Phys.* **2015**, *48*, 184002.

(43) McPeak, K. M.; Jayanti, S. V.; Kress, S. J. P.; Meyer, S.; Iotti, S.; Rossinelli, A.; Norris, D. J. *ACS Photonics* **2015**, *2*, 326–333.

(44) Duan, H.; Manfrinato, V. R.; Yang, J. K. W.; Winston, D.; Cord, B. M.; Berggren, K. K. *J. Vac. Sci. Technol. B* **2010**, *28*, C6H11.

(45) Hobbs, R. G.; Yang, Y.; Keathley, P. D.; Swanwick, M. E.; Velásquez-Garcíia, L. F.; Kärtner, F. X.; Graves, W. S.; Berggren, K. K. *Nanotechnology* **2014**, *25*, 465304.

(46) van Oven, J. C.; Berwald, F.; Berggren, K. K.; Kruit, P.; Hagen, C. W. *J. Vac. Sci. Technol. B* **2011**, *29*, 06F305.

(47) Duan, H.; Winston, D.; Yang, J. K. W.; Cord, B. M.; Manfrinato, V. R.; Berggren, K. K. *J. Vac. Sci. Technol. B* **2010**, *28*, C6C58.

(48) Mecklenburg, M.; Hubbard, W. A.; White, E. R.; Dhall, R.; Cronin, S. B.; Aloni, S.; Regan, B. C. *Science* **2015**, *347*, 629–633.

(49) Manfrinato, V. R.; Wen, J.; Zhang, L.; Yang, Y.; Hobbs, R. G.; Baker, B.; Su, D.; Zakharov, D.; Zaluzec, N. J.; Miller, D. J.; Stach, E. A.; Berggren, K. K. *Nano Lett.* **2014**, *14*, 4406–4412.

(50) Manfrinato, V. R.; Zhang, L.; Su, D.; Duan, H.; Hobbs, R. G.; Stach, E. A.; Berggren, K. K. *Nano Lett.* **2013**, *13*, 1555–1558.

(51) Yang, J. K. W.; Berggren, K. K. *J. Vac. Sci. Technol. B* **2007**, *25*, 2025.

(52) Alber, I.; Sigle, W.; Muller, S.; Neumann, R.; Picht, O.; Rauber, M.; van Aken, P. A.; Toimil-Molares, M. E. *ACS Nano* **2011**, *5*, 9845.

(53) Bellido, E. P.; Manjavacas, A.; Zhang, Y.; Cao, Y.; Nordlander, P.; Botton, G. A. *ACS Photonics* **2016**, No. 3, 428–433.

(54) Alber, I.; Sigle, W.; Demming-Janssen, F.; Neumann, R.; Trautmann, C.; van Aken, P. A.; Toimil-Molares, M. E. *ACS Nano* **2012**, *6*, 9711–9717.

(55) Scholl, J. A.; Koh, A. L.; Dionne, J. A. *Nature* **2012**, *483*, 421–427.

(56) Nelayah, J.; Kociak, M.; Stéphan, O.; García de Abajo, F. J.; Tencé, M.; Henrard, L.; Taverna, D.; Pastoriza-Santos, I.; Liz-Marzán, L. M.; Colliex, C. *Nat. Phys.* **2007**, *3*, 348–353.

(57) Li, G.; Cherqui, C.; Bigelow, N. W.; Duscher, G.; Straney, P. J.; Millstone, J. E.; Masiello, D. J.; Camden, J. P. *Nano Lett.* **2015**, *15*, 3465–3471.

(58) Aizpurua, J.; Rivacoba, A. *Phys. Rev. B* **2008**, *78*, 035404.

(59) Christensen, T.; Yan, W.; Raza, S.; Jauho, A.-P.; Mortensen, N. A.; Wubs, M. *ACS Nano* **2014**, *8*, 1745–1758.

(60) Schmidt, F. P.; Ditlbacher, H.; Hohenester, U.; Hohenau, A.; Hofer, F.; Krenn, J. R. *Nano Lett.* **2012**, *12*, 5780–5783.

(61) Krug, M. K.; Reisecker, M.; Hohenau, A.; Ditlbacher, H.; Trügler, A.; Hohenester, U.; Krenn, J. R. *Appl. Phys. Lett.* **2014**, *105*, 171103.

(62) Coronado, E. A.; Schatz, G. C. *J. Chem. Phys.* **2003**, *119*, 3926.

(63) Kreibig, U. *J. Phys. F Met. Phys.* **1974**, *4*, 999–1014.

(64) Egerton, R. F. *Electron Energy-Loss Spectroscopy in the Electron Microscope*, 3rd ed.; Springer: New York, 2011.

(65) Barrera, R. G.; Fuchs, R. *Phys. Rev. B* **1995**, *52*, 3256–3273.

(66) Haberfehlner, G.; Trugler, A.; Schmidt, F. P.; Horl, A.; Hofer, F.; Hohenester, U.; Kothleitner, G. *Nano Lett.* **2015**, *15*, 7726–7730.

(67) Krysak, M.; Trikeriotis, M.; Schwartz, E.; Lafferty, N.; Xie, P.; Smith, B.; Zimmerman,

P.; Montgomery, W.; Giannelis, E.; Ober, C. K. *Proc. SPIE* **2011**, *7972*, 79721C.

(68) Neisser, M.; Cummings, K.; Valente, S.; Montgomery, C.; Fan, Y.-J.; Matthews, K.; Chun, J.; Ashby, P. D. *Proc. SPIE* **2015**, *9422*, 94220L.

(69) Raether, H. *Springer Tracts Mod. Phys.* **1980**, *88*, 1–180.

Table of Contents Graphic